

Independent Continuous Tracking of Multiple Agents in the Human Hippocampus

Assia Chericoni¹, Justin M. Fine¹, Ana G. Chavez¹, Melissa C. Franch¹, Elizabeth A. Mickiewicz¹, Raissa K. Mathura¹, Joshua Adkinson¹, Eleonora Bartoli¹, Joshua Jacobs², Nicole R. Provenza¹, Andrew J. Watrous¹, Seng Bum Michael Yoo³, Sameer A. Sheth¹, and Benjamin Y. Hayden¹

1. Department of Neurosurgery, Baylor College of Medicine, Houston, Texas,
United States of America
2. Department of Biomedical Engineering, Columbia University
3. Institute for Basic Science (IBS), Sungkyunkwan University, South Korea

* Correspondence: Benjamin.Hayden@bcm.edu

Funding statement

This research was supported by the McNair Foundation, by NIH R01 MH129439, R01 DA038615 and U01 NS121472.

Competing interests

S. A. S. has been consultant for Boston Scientific, Zimmer Biomet, Abbott, Koh Young, Neuropace and is co-founder of Motif Neurotech.
The other authors have no competing interest to declare.

Acknowledgements

We thank George Kokalas and Victoria Gates for invaluable assistance.

28

ABSTRACT

29 The pursuit of fleeing prey is a core element of many species' behavioral repertoires. It
30 poses the difficult problem of continuous tracking of multiple agents, including both self and
31 others. To understand how this tracking is implemented neurally, we examined responses of
32 hippocampal neurons while humans performed a joystick-controlled continuous prey-pursuit task
33 involving two simultaneously fleeing prey (and, in some cases, a predator) in a virtual open field.
34 We found neural maps encoding the positions of all the agents. All maps were multiplexed in
35 single neurons and were disambiguated by the use of the population coding principle of semi-
36 orthogonal subspaces, which can facilitate cross-agent generalization. Some neurons, more
37 common in the posterior hippocampus, had narrow tuning functions reminiscent of place cells,
38 lower firing rates, and high information per spike; others, which were found in both anterior and
39 posterior hippocampus, had broad tuning functions, higher firing rates, and less information per
40 spike. Semi-orthogonalization was selectively associated with the broadly tuned neurons. These
41 results suggest an answer to the problem of navigational individuation, that is, how mapping
42 codes can distinguish different agents, and establish the neuronavigational foundations of
43 pursuit.

44

INTRODUCTION

45 Pursuit is a foraging behavior involving continuous and interactive navigation with the
46 goal of catching a fleeing prey while avoiding predators (Fabian et al., 2018; Olberg et al., 2000;
47 Stephens & Krebs, 1986; Ydenberg & Dill, 1986). It is an archetypal example of continuous
48 decision-making, in which choice and control are deployed simultaneously (Burge et al., 2025;
49 Cisek and Kalaska, 2010; Gordon et al., 2021; Merel et al., 2015; Yoo et al., 2021A). Moment to
50 moment choices during pursuit require tracking the locations of multiple agents at the same time,
51 including the self, pursued prey, and unpursued prey, and navigating towards interception loci.

52 Among regions associated with navigation, the hippocampus is the most well studied
53 (Chersi and Burgess, 2015; Ekstrom et al., 2018; Epstein et al., 2017; Kunz et al., 2021; Maguire
54 et al., 2006; Nyberg et al., 2022; O'Keefe and Dostrovsky, 1971; Suthana et al., 2009). The
55 hippocampus contains place cells that track the allocentric position of the self in physical space
56 (Ekstrom et al., 2003; Jacobs et al., 2010; Miller et al., 2013; O'Keefe et al., 1998; Wilson and
57 McNaughton, 1993) and virtual space (Harvey et al., 2009; Mackay et al., 2024). The
58 hippocampus also has a variety of other neurons relevant to pursuit (Behrens et al., 2018). These
59 include neurons that are tuned to positions of external (physical) goals (Brown et al., 2016;
60 Gauthier and Tank, 2018; Kunz et al., 2021; Poucet and Hok, 2017; Watrous et al., 2018), and
61 'social' place cells that track the positions of other agents (Danjo et al., 2018; Forli and Yartsev,
62 2023; Omer et al., 2018; Rao et al., 2019; Stangl et al., 2021; Zang et al., 2024). The collective
63 existence of these neurons indicates that the hippocampus contains the basic ingredients to track
64 both self and prey in the course of pursuit. However, it does not give insight into how the brain
65 solve the problem of disambiguating representations when faced with multiple distinct agents.

66 The need to distinguish self from others, and to distinguish multiple others, means that
67 the brain must solve the *individuation problem*. In short, the brain needs a mechanism to know
68 which agent a neuron's responses refer to. One possibility would involve labelled line coding, in
69 which separate sets of neurons track each single agent. However, such codes tend to be inflexible
70 and have limited capacity for generalization (Barak et al., 2013; Fine et al., 2023; Fusi et al.,
71 2016). In addition to these theoretical concerns, there are empirical ones: most brain areas
72 contain mixed selective codes rather than labeled line codes (Ebitz and Hayden 2021; Fusi et al.,
73 2016; Rigotti et al., 2013; Tye et al., 2024). One way for the brain to handle disambiguation of
74 maps for distinct agents, despite the mixed selectivity, is to represent the maps in semi-

75 orthogonal population subspaces (Elsayed et al., 2016; Johnston et al., 2024; Kaufman et al.,
76 2022; Parthasarathy et al., 2017; Tang et al., 2020; Xie et al., 2022; Yoo and Hayden, 2020).
77 Here, we tested the hypothesis that the hippocampus uses subspace semi-orthogonalization to
78 individuate maps related to distinct agents during continuous pursuit.

79 We recorded populations of neurons in the hippocampus in thirteen humans performing
80 a virtual pursuit task with two prey and (in a subset of participants) a predator. We found neurons
81 that encode position maps of the self, both prey, and the predator. Some neurons encoded the
82 position of one agent, but the majority were mixed selective for multiple agents; in these mixed
83 selective neurons, maps for different agents were largely unrelated. We found these hippocampal
84 maps can be readily separated into two types: one with narrow spatial extent, reminiscent of
85 place cells, and one with broader less-localized tuning. Narrowly tuned neurons were more
86 prevalent in the posterior hippocampus and encoded position more efficiently, exhibiting greater
87 spatial information per spike despite diminished firing rates, compared to broadly tuned neurons.
88 Notably, the population used subspace semi-orthogonalization for different agents; this coding
89 principle was observed primarily in the broadly tuned neurons. Thus, rather than relying on
90 labeled-line coding, the hippocampus appears to individuate multiple agents through population-
91 level subspace organization, allowing for flexible encoding of distinct yet overlapping spatial
92 representations.

93

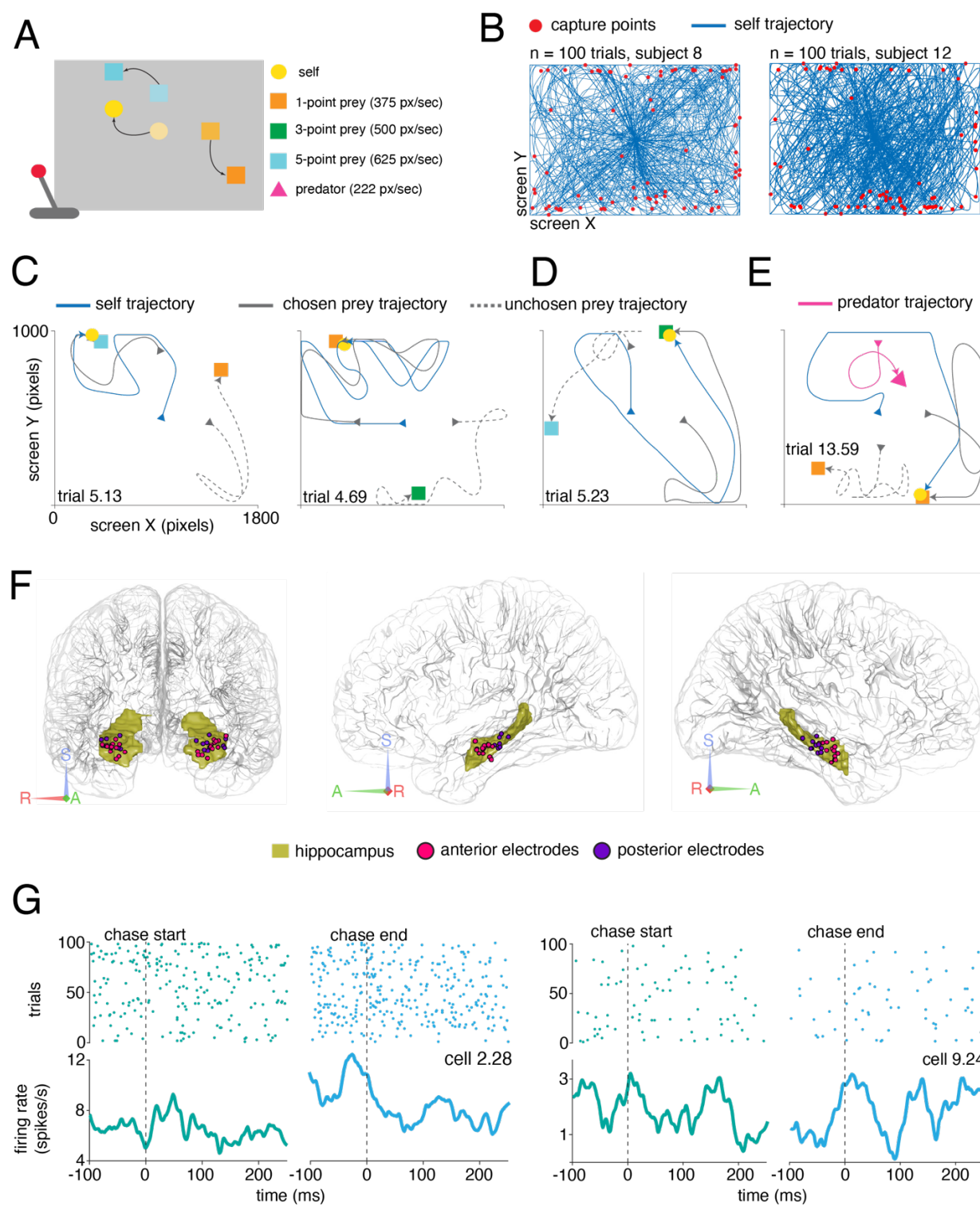
RESULTS

94 Prey pursuit in humans

95 Human participants ($n=13$) performed the *prey-pursuit task* (**Figure 1A, Methods**; Yoo
96 et al., 2020). On each trial, the participant used a joystick to continuously move the position of
97 an avatar (yellow circle) in a rectangular field displayed on a computer screen (**Supplementary**
98 **Video, Figure 1A and B**). The participant had up to 20 seconds to capture fleeing prey (colored
99 squares) to obtain points. Prey avoided the avatar with a deterministic strategy that combined
100 repulsion from the avatar's current position with repulsion from the walls of the field (**Methods**).
101 The prey items were drawn randomly on each trial from a set of three that differed in maximum
102 velocity and reward size.

103 Each trial began with one or two prey appearing at one of the cardinal points (**Figure**
104 **1A**). In two-prey trials (81% of trials), the participant was free to decide which prey to pursue at
105 any moment (**Figure 1C, D**). Participants successfully captured the prey in 73.72% of trials and,
106 on successful trials, did so in an average of 7.51 seconds (variance: 1.67 seconds) with an
107 average reaction time of 0.87 seconds (variance: 0.01 seconds), measured as the interval between
108 the agents' appearance on the screen and the participant's first move. Participants' performance
109 did not depend significantly on prey type (trial length x reward level, $p = 0.16$; reaction time x
110 reward level, $p = 0.51$). In three participants, we employed a variant of the task in which, in
111 addition to the prey, there were also predators pursuing the participant's avatar (**Figure 1E**). In
112 this case, the predator used a simple distance-minimizing pursuit strategy. Our participants
113 successfully evaded capture by the predator in 91.67% of trials.

114 We recorded responses of 390 neurons in the hippocampus while participants performed
115 this task (average $n=30$ neurons per participant). Of these neurons, 96 were also recorded in the
116 variant of the task with a predator. Of all 390 neurons, roughly half ($n=199$) were in anterior
117 hippocampus and the remainder ($n=191$) were in posterior hippocampus (**Figure 1F**). We
118 defined the border between these regions as a coronal plane along the longitudinal hippocampal
119 axis ($y = -20$, MNI). This border is largely consistent with that used in previous studies (e.g.,
120 Poppenk et al., 2013). Average firing rates aligned to trial stop and start show some intriguing
121 patterns (**Figure 1G**). Overall, however, neurons had complex selectivities that were not readily
122 explainable in terms of trial start and stop. We therefore examined responses as a function of
123 location of each agent in the virtual space of the task.



124
125 **Figure 1. Task design and neural recordings. A,** Schematic of the prey-pursuit task.
126 Participants use a joystick to control the position of an avatar (yellow circle) on a computer
127 screen to capture prey (squares) and score points. For some participants, we also included
128 predators (**Methods**). **B,** Example sessions from two participants; blue lines indicate

129 participants' trajectories on each trial overlaid; red dots indicate points of prey capture. **C, D, E,**
130 Typical example trials from different participants. Trials are identified as *participant number.trial*
131 *number*. Continuous gray lines indicate the chosen prey trajectories and dashed gray lines the
132 unchosen prey trajectories. Predators' trajectories are reported in magenta. **D**, Example trial in
133 which the participant switched from pursuing one prey to another. **E**, Example of trial with
134 predator - capture from the predator leads to point loss. **F**, Recording sites of hippocampal
135 neurons from all 13 participants. Recording sites within the anterior hippocampus are reported
136 in magenta while recording sites within the posterior hippocampus in purple. **G**, Peri-stimulus
137 time histograms and raster plots demonstrating responses to chase start and chase end from
138 two hippocampal neurons from participant 2 (left column) and participant 9 (right column).
139 Dashed vertical lines represent the beginning and the end of the chase. Plots display mean
140 firing rates.
141
142

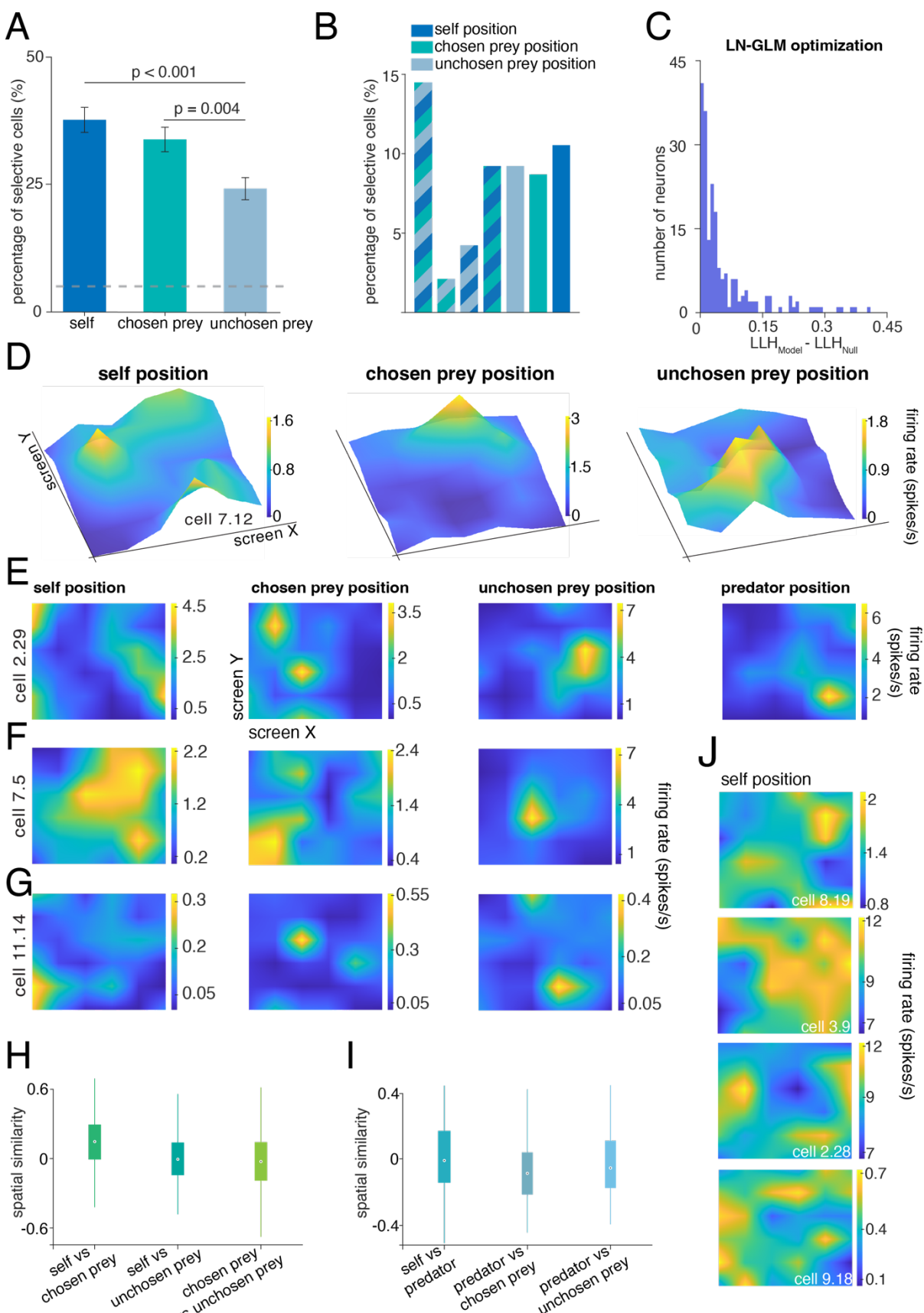
143 Hippocampal maps for positions of self, prey, and predators

144 To estimate mapping functions in these neurons, we used the Poisson generalized linear
145 model procedure developed by Hardcastle et al. (2017). This approach fits tuning models to
146 neuronal responses without any a priori assumptions about the shape of the tuning surface. For
147 this analysis, and all the subsequent ones, we concatenated all the successful trials involving two
148 prey. (Single prey trials showed similar results and are not described here). To describe our
149 results here, we use the term *chosen prey* for the prey that was ultimately captured, while the
150 other was the *unchosen prey* (**Figure 1C, D**).

151 We found 37.7% (n=147/390) of neurons map the position of the self, while 33.9%
152 (n=132/390) map the position of the chosen prey, and 24.4% (n=95/390) map the position of the
153 unchosen prey (**Figure 2A, B, D, F, G**). In the neurons that we recorded during predator trials,
154 27.08% (n=26/96) map the position of the predator (**Figure 2E**). We found that 15.1%
155 (n=59/390) of the neurons encode the position of any two agents, and 14.4% (n=56/390) map all
156 three agents (**Figure 2B**). Similarly, during predator trials, 15.6% of the neurons (n=15/96) map
157 the position of two or three agents, with 8.3% (8/96) mapping the position of all four agents.
158 These proportions are all higher than would be expected by chance ($p < 0.001$, binomial test).

159 Next, we asked whether hippocampal neurons have different maps for the different
160 agents. To quantify the relationship between maps, we used a *spatial similarity index* (SPAECF,
161 Koch et al., 2018, **Methods**), which measures the correlation between spatial representations. A
162 value of zero indicates full orthogonality between maps, while values closer to +1 or -1, indicate
163 correlation or anti-correlation between maps, respectively.

164 The mean spatial similarity between self and chosen prey maps is 0.14. This value is very
165 low, but is nonetheless greater than zero ($p = 0.002$, **Figure 2H, Methods**) and below noise
166 ceiling ($p < 0.001$). Thus, these maps appear to be largely, but not entirely distinct. The mean
167 spatial similarity between self and unchosen prey maps is even lower, but is still different from
168 zero (SPAEC = 0.002, $p < 0.001$, **Figure 2H**). The chosen and unchosen prey maps are weakly,
169 but significantly anti-correlated (SPAEC = -0.02, $p = 0.001$, **Figure 2H**). Also in this case, both
170 values were below noise ceiling ($p < 0.001$). Finally, in the subset of neurons in which we had
171 predator data, we found that the spatial similarity between self and predator was again slightly
172 positive but not different from zero (SPAEC = 0.006, $p = 0.79$, **Figure 2I**). These single-neuron
173 SPAEC results are reminiscent of the idea of semi-collinearity, in which coding at the population
174 level shows a mixture of orthogonality and collinearity (Johnston et al., 2024). We therefore next
175 tested this population level idea directly.



177 **Figure 2. Hippocampal mapping functions for self and prey.** **A**, Bar plot showing the
178 percentage of neurons tuned to agent positions according to the LN-GLM approach. In total
179 51.79% (202/390) of the neurons were selective for any of the agents' positions. Proportions do
180 not sum up to hundred as one neuron may be tuned to more than one agent's position. Dashed
181 horizontal grey line represents chance level, which is 5%. Error bars represent standard errors.
182 Significance was determined using a chi-square test for proportions, with a significance
183 threshold of 0.05. **B**, Barplot showing the proportion of neurons tuned to more than one agent's
184 position. For instance, the first bar from the left shows that 14.36% of the neurons were
185 selective for the position of all three agents. **C**, Quantification of model performance using log-
186 likelihood (LLH) increase. The histogram shows LLH increase values for neurons significantly
187 tuned to at least one agent's position. LLH increase was computed as the improvement over a
188 null model assuming a constant firing rate, using 10-fold cross-validation. Only neurons where
189 the best-fit model significantly outperformed the null model (Wilcoxon signed-rank test, $p < 0.05$)
190 are shown. LLH increase values were normalized by spike count and converted to bits per spike
191 using log base 2 scaling. **D, E, F, G**, Three-dimensional (top row) and two-dimensional (bottom
192 rows) representations of spatial firing rate maps for neurons significantly tuned to the position of
193 all the agents. Each row corresponds to a single neuron, while each column represents the
194 firing activity relative to different agents (self, chosen prey, unchosen prey, and predator when
195 present). Yellower regions indicate locations where the neuron exhibited higher firing rates.
196 Data points were interpolated for visualization purposes only. **H**, Boxplots representing the
197 median spatial similarity between maps across different agent representations, errorbars
198 represent the standard error. Spatial similarity values near zero indicate orthogonality (low
199 similarity) between maps. All the neurons are shown. **J**, Example maps from neurons that were
200 significantly tuned to self position.

201
202

203 **Narrow and broad tuning curves for spatial position**

204 We next surveyed the distribution of tuning curve shapes. Some hippocampal neurons
205 have selectivity for positions that are localized to a specific location, akin to the narrow maps of
206 place cells (**Figure 2D, E, G**). However, others have broader response functions that are not as
207 narrowly localized, but that nonetheless carry strong spatial information (**Figure 2F, J**).

208 We performed a k-means clustering of self-position tuning functions (**Methods**). We
209 validated the clustering output using silhouette scores, which can provide an estimate of the most
210 likely number of true clusters (Rousseeuw, 1987). This analysis shows that only two clusters are
211 needed (mean silhouette value = 0.6, **Figure 3A, B**). In our population of neurons, 70.5%
212 ($n=275/390$) belong to cluster 1 (C1) which has neurons with broad spatial tuning; the remaining
213 29.5% ($n=115/390$) are in cluster 2 (C2), which has neurons with narrow place cell-like tuning
214 (**Figure 3A, B**).

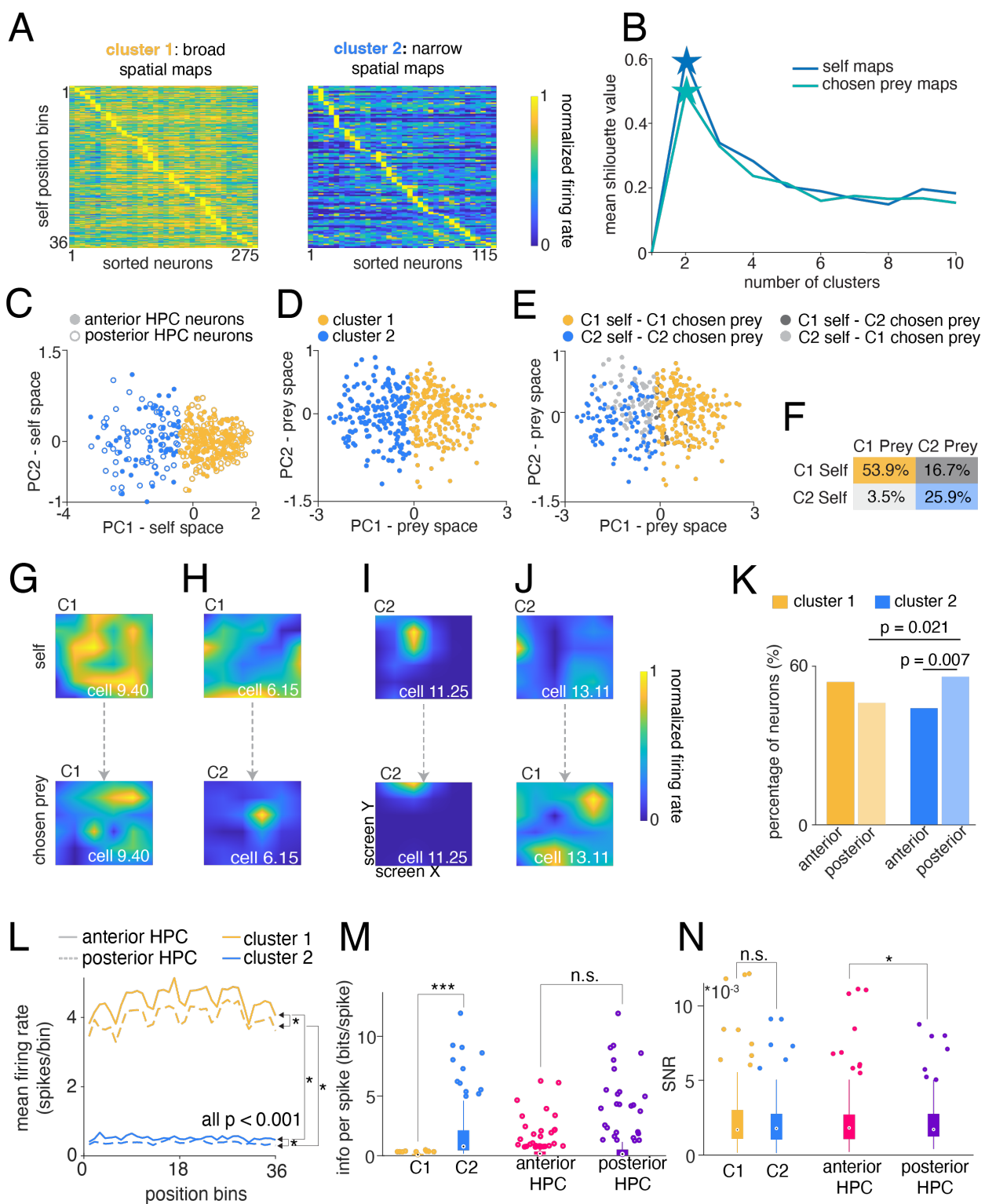
215 We applied principal component analysis (PCA) on the self-position tuning functions and
216 visualized the population distribution in a lower dimensional space (**Methods**). Neurons
217 belonging to cluster 1 and cluster 2 are clearly separable along the first principal component
218 (PC1), which represents the overall *spatial extent* of the tuning, while the second principal
219 component (PC2) may capture differences in neurons' preferred firing locations, signifying
220 *spatial preference* (**Figure 3C**). Indeed, neurons with broad spatial representations are
221 distributed on the right side of PC1, with little variability along both PC1 and PC2, which may
222 indicate greater spatial extent and lower spatial preference. That is, firing patterns are more
223 widespread and heterogeneous across multiple spatial locations (**Figure 3C**). In contrast, neurons
224 with narrow spatial representations were more dispersed along both PC1 and PC2, reflecting
225 greater variability in their tuning peaks - spatial extent - and spatial preference (**Figure 3C**).

226 We performed the same clustering procedure, but this time using chosen prey's position
227 tuning functions (**Methods**). As with self-position, the silhouette test showed optimal results
228 with $k = 2$ (mean silhouette value = 0.5, **Figure 3B**), confirming that population response relies
229 on broad and narrow maps to represent position (**Figure 3D**). For these chosen prey maps, we
230 found that 57.44% ($n=224/390$) belong to cluster 1, while the remaining 42.56% ($n=166/390$)
231 belong to cluster 2. The overwhelming majority of neurons (79.80%) consistently fall into the
232 same cluster for self- and prey-position (**Figure 3E, F, G, I**), whereas the remaining 20.20% of
233 neurons switch between broad and narrow spatial maps (**Figure 3E, F, H, J**). Repeating the
234 same analysis on both self and chosen prey maps, first applying PCA followed by k-means
235 clustering, yielded similar results.

236 We found that broad and narrow neuron maps are differentially distributed along the
237 longitudinal axis of the hippocampus. Specifically, we observed a greater preponderance of
238 broadly tuned neurons in the anterior hippocampus and a greater preponderance of neurons with
239 narrow spatial tuning in the posterior hippocampus (**Figure 3K**). Among cluster 1 neurons,
240 53.80% localized rostrally with the remaining 46.20% caudally, with no significance difference
241 between them (one sample z-test for proportions: $p = 0.99$). Among cluster 2 neurons, 44.30%
242 are found rostrally and 55.70% caudally. While this difference is modest, it is statistically
243 significant (one sample z-test for proportions: $p = 0.007$; **Figure 3K**). This result remained
244 unchanged even when considering only the significantly tuned neurons. Out of the cluster 2
245 tuned neurons, 42.10% localize in the anterior hippocampus and 57.90% in the posterior (one

246 sample z-test for proportions: $p = 0.003$; data not shown). Moreover, within the posterior
247 hippocampus, we found a higher proportion of cluster 2 neurons compared to cluster 1 (one
248 sample z-test for proportions: $p = 0.021$; **Figure 3K**). Within the anterior hippocampus, instead,
249 there was no significant difference between the proportion of cluster 1 and cluster 2 neurons (one
250 sample z-test for proportions: $p = 0.98$, **Figure 3K**). Together, these results confirm theories that
251 anterior and posterior hippocampus have measurable functional differences.

252 Last, we examined how these two distinct categories of neurons fire across space along
253 with the associated signal-to-noise ratio (SNR), defined as the tuning curve variance normalized
254 by firing rate (**Methods**). We found that neurons carrying broad spatial representation exhibit
255 higher firing rates but carry less spatial information compared to narrowly tuned neurons
256 (ranksum, $p < 0.001$; **Figure 3L, M**). Nonetheless, the SNR remained comparable across clusters
257 (**Figure 3N**), indicating that the firing rate and information per spike roughly cancelled each
258 other out. However, we did find that neurons in the posterior hippocampus had lower firing rates
259 but higher SNR compared to anterior hippocampal neurons (**Figure 3L, N**). These findings
260 highlight distinct encoding strategies along the longitudinal hippocampal axis.



261
262

263 **Figure 3. Hippocampal tuning profiles are heterogeneous. A,** Heatmaps depicting
264 the two clusters of neurons identified using k-means clustering. Each matrix represents unfolded
265 neuron maps, where rows correspond to position bins and columns to individual neurons.
266 Neurons are sorted according to their peak firing positions (bins). Firing rates are normalized

267 within neurons between 0 and 1. **B**, Silhouette scores used to assess clustering quality and
268 determine the optimal number of clusters for both self and chosen prey maps. Stars indicate the
269 selected number of clusters. **C**, Neurons projected onto the PC space derived from self-position
270 maps, colored according to k-means clustering performed on self maps. **D**, Same as in C, but
271 PCA and k-means were performed on chosen prey maps. **E**, Neurons projected onto the
272 chosen prey PCs space, now colored by cross-referencing k-means clustering results from self
273 and chosen prey maps. **F**, Proportion of neurons assigned to each cluster based on their self
274 and chosen prey representation. The table highlights the percentage of neurons that remained
275 in the same cluster across self and chosen prey representations, as well as those that switched
276 clusters between conditions. **G, H, I, J**, Example neurons demonstrating shared (G, I) or distinct
277 (H, J) spatial representations for self and chosen prey. Each column corresponds to a single
278 neuron, with the top rows showing spatial tuning to self and the bottom row tuning to chosen
279 prey. **K**, Comparison of neuron distribution between anterior and posterior hippocampus across
280 clusters. Significance is based on one sample z-test for proportions. **L**, Plot representing the
281 mean firing rate across a 6x6 grid (36 bins - x axis). All p < 0.001, Wilcoxon rank sum test. **M**,
282 Boxplot representing the spatial information per spike computed as the mutual information
283 between the spatial location and the spike train, p < 0.001, Wilcoxon rank sum test. **N**, Boxplot
284 representing the SNR computed as the ratio between the variance of the tuning and the
285 average firing rate, where a higher SNR means a neuron fires more reliably in specific locations;
286 p = 0.02, Wilcoxon rank sum test.
287
288

289 Hippocampal neurons use semi-orthogonal maps to disambiguate agents

290 Theoretical and empirical data support the idea that neural populations can use
291 orthogonal neural subspaces to partition information encoded in the same neurons (Ebitz and
292 Hayden, 2021; Elsayed et al., 2016; Kaufman et al., 2022; Panichello and Buschman, 2021; Tang
293 et al., 2020; Xie et al., 2022; Yoo and Hayden, 2020). Moreover, blending orthogonal and
294 collinear subspaces, producing semi-orthogonal subspaces, allows for discrimination while
295 enabling cross-categorical generalization (**Figure 4A-D**; Barak et al., 2013; Bernardi et al., 2020;
296 Johnston et al., 2024).

297 To test the hypothesis that hippocampal neural populations use semi-orthogonal
298 subspaces to disentangle agents' maps, we adapted a method previously developed to study
299 motor regions (Elsayed et al., 2016). This analysis quantifies the degree of overlap between
300 spatial representations for self and prey, by projecting the population activity onto low-
301 dimensional subspaces that capture most of the variance between agents' representations
302 (**Methods**). We applied this analysis separately to both clusters. We found that neurons with
303 broad spatial maps (cluster 1) use distinct, semi-orthogonal subspaces to individuate agents'

304 locations. We also found that neurons with narrow spatial maps (cluster 2) represent self and
305 prey on nearly collinear subspaces.

306 In more detail, we started by analyzing the correlation structure for self and prey
307 representations. For each agent, we computed the spatial similarity between the tuning surfaces
308 for each pair of neurons (**Figure 4E, F**). Each entry in the resulting *spatial similarity matrix*
309 represents the degree of spatial similarity between the response patterns of two neurons. For C1
310 neurons, the matrix structure changes markedly across agents (**Figure 4E**), whereas for C2
311 neurons, it remains largely consistent (**Figure 4F**). Indeed, when we compared the entries of the
312 self matrix against the entries of the prey matrix, we found little or no correlation (C1: not
313 different from chance, determined by pseudocorrelation, self vs chosen prey: $R^2 = 0.19 \pm 0.040$,
314 $p = 0.46$; self vs unchosen prey: $R^2 = 0.06 \pm 0.039$, $p = 0.99$; two-sided permutation test, $\alpha =$
315 0.05; **Figure 4G**; C2: self vs chosen prey: $R^2 = 0.19 \pm 0.037$, $p < 0.001$; self vs unchosen prey:
316 $R^2 = 0.14 \pm 0.038$, $p = 0.006$, **Figure 4H**). Thus, for a pair of neurons with broad spatial maps
317 (cluster 1), the similarity of their responses to self-locations does not inform the similarity of
318 their responses to prey locations. A possibility is that these neurons individuate agents in space
319 with some dimensions dedicated to self-only, some to prey-only, and some to both - aligning
320 with the hypothesis of semi-orthogonality between neural subspaces.

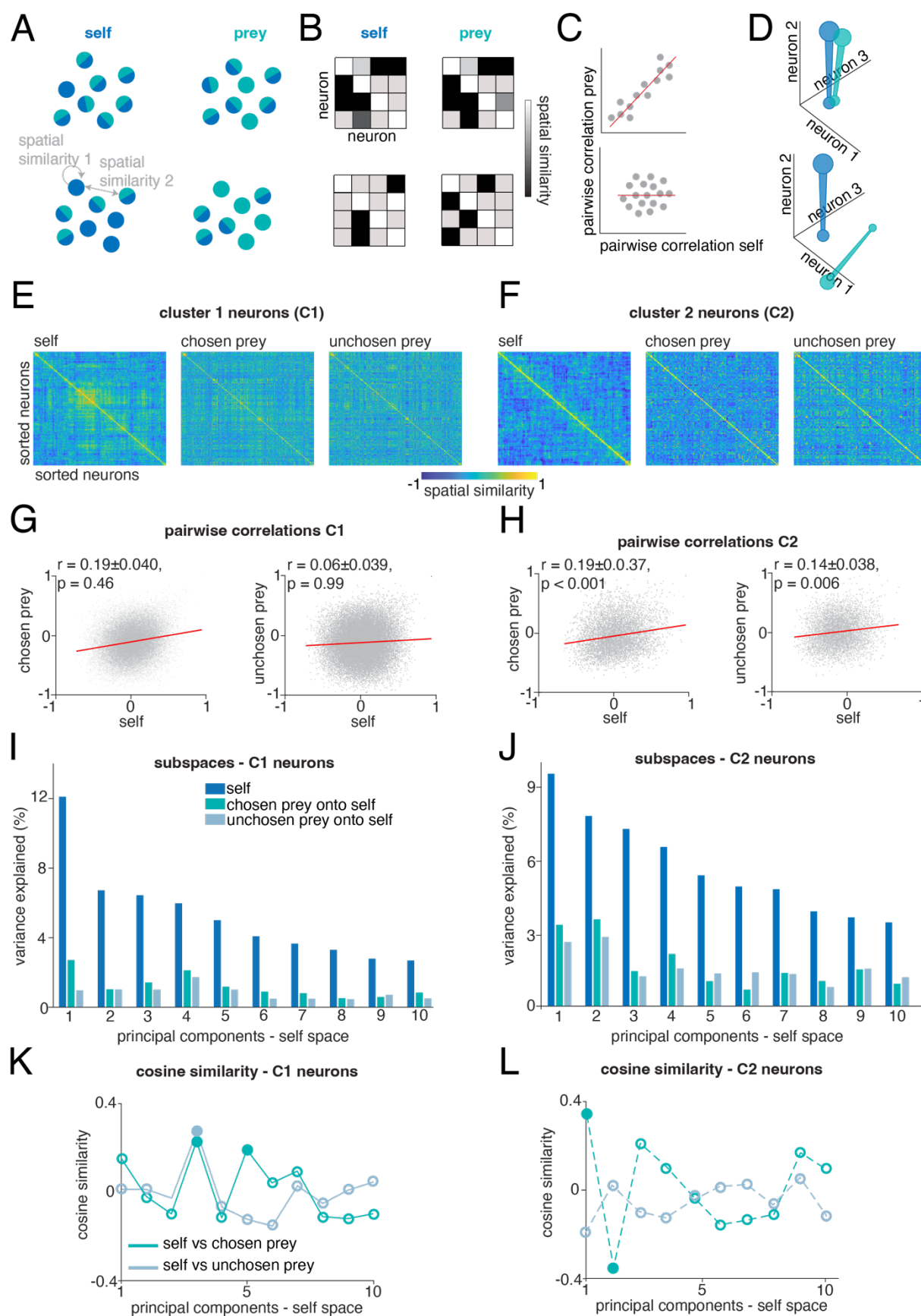
321 To understand if these subspaces were semi-orthogonal, we applied eigendecomposition
322 to the self spatial similarity matrix and individuated the top self-principal components (PCs). If
323 self and prey maps are semi-orthogonal, the self-PCs should capture very little prey variance
324 (**Methods**). To assess if self-PCs can significantly capture the prey maps variance, we computed
325 variance explain noise ceiling and confidence intervals through half-split cross-validation (CV)
326 (**Methods**). For each split, we used half of the self spatial maps (train half) to compute the self-
327 PCs. We then use these self-PCs to project the test half's spatial maps for both self (within-self
328 variance) and prey (cross-agents variance). The distribution of within-self variances gives an
329 estimate of noise ceiling, while the cross-agents variance explained quantifies how well self-PCs
330 capture prey maps variance. The variability of both within-self and across-agents variance
331 provides confidence intervals for each agent's projections.

332 For cluster 1 neurons, we found that the prey variance explained was significantly lower
333 than noise ceiling ($p < 0.001$, for PC1 to PC10), though confidence intervals did not overlap
334 between self and prey projections for PC1 only. That is, self-PC1 carries information unique to

335 the self maps. Overlapping confidence intervals for the remaining components implied that self
336 and prey representations share non-zero variance (**Figure 4I**).

337 Lastly, to estimate the degree of orthogonality between agents' neural subspaces, we
338 identified the top prey-PCs, and estimated the cosine similarity between self and prey -PCs. A
339 value of cosine similarity close to zero means orthogonality, while values closer to 1 or -1
340 collinearity. The cosine similarity values between the self-PCs and prey-PCs, fluctuate around
341 zero, confirming weak alignment between PCs, i.e., semi-orthogonality between subspaces
342 (**Figure 4K**). In summary, these results tell us that neurons with broad spatial tuning individuate
343 prey and self using semi-orthogonal neural subspaces.

344 The same decomposition analysis performed on neurons with sparse spatial tuning
345 (cluster 2), yielded slightly different results. Given the significant correlations between self and
346 prey representations, a potential explanation is that agents lie on collinear subspaces. We found
347 that also in this case, the prey variance explained is significantly lower than noise ceiling ($p <$
348 0.001, for PC1 to PC10), but confidence intervals overlap across all the PCs, indicating shared
349 variance between self and prey maps (**Figure 4J**). The cosine similarity between the top two
350 self-PCs and chosen prey-PCs significantly differs from zero (PCs1: 0.78, $p = 0.02$; PCs2: -0.36,
351 $p = 0.04$, **Figure 4L**). Our results indicate that neurons with narrow spatial maps represent self
352 and prey in nearly collinear subspaces, and that subspace semi-orthogonalization in hippocampal
353 neurons is primarily driven by neural populations with broad spatial tuning.



355 **Figure 4. Neural subspaces allow for agent generalization. A, B, C, D,** Schematic of neural
356 subspaces orthogonalization. **A**, Cartoon showing activity of ensemble neurons. Each neuron
357 maps the position of one or more agents. **B, C**, Spatial similarity matrix and pairwise correlation;
358 uncorrelated activity results in subspace orthogonalization (bottom row) and vice versa (upper
359 row). **D**, Blue represents the self subspace, while green represents the prey subspace.
360 Correlated neural activity results in collinear subspaces (top row) and viceversa (bottom row). **E**,
361 Spatial similarity matrices for all the possible neuron pairs in cluster 1 for self and prey. Neurons
362 of each matrix are sorted using a hierarchical clustering algorithm applied on the self matrix
363 only. Z axis indicates the strength of correlation between the overall average activities of
364 neurons pairs. Lack of obvious structure in the self matrix reflects strong functional
365 reorganization between self and prey. **F**, Same as in E, but for cluster 2 neurons. **G**, Pairwise
366 correlation for each pair of neurons in cluster 1 for self and prey. The lack of correlation
367 indicates that the relationship between neurons changes across agents. Reported values
368 indicate Pearson's correlation coefficient with 95% confidence intervals, and permutation-based
369 p-values were computed using a two-tailed test, with significance considered at $p < 0.05$. **H**,
370 Same as in E, but significant correlations indicate that the relationship between neuron pairs in
371 cluster 2 is preserved across agents, suggesting a shared representational structure. **I**, Percent
372 variance explained by each of self-PCs for prey maps projected onto the self. The low height of
373 the green and grey bars relative to the blue ones illustrates the poor match between self and
374 prey subspaces. **J**, As in I, but for cluster 2 neurons. **K**, Cosine similarity between self and prey
375 PCs, values closer to zero indicate orthogonality between PCs. Filled dots represent nonzero
376 values (two-tailed test, with significance considered at $p < 0.05$). **L**, as in K, but for cluster 2
377 neurons.

378

DISCUSSION

379 Here we find, in a virtual prey pursuit task, that neurons in the human hippocampus can
380 track positions of multiple agents (self, two prey, and a predator) simultaneously using distinct
381 maps. Rather than use a labelled line code (in which a given neuron's responses correspond to
382 the position of a single agent), maps are multiplexed. This multiplexing of information raises an
383 *individuation problem*: if firing rate of a neuron changes, which of the tracked agents does that
384 change refer to? Our data suggest that the hippocampus solves this problem by recourse to *semi-*
385 *orthogonal subspaces*, which blend orthogonal and collinear subspaces. Subspace partition
386 allows for simultaneous separation of information (thus solving the individuation problem) while
387 also allowing for cross-agent generalization, greatly facilitating flexible learning (Barak et al.,
388 2013; Fusi et al., 2016; Johnston et al., 2024). These results, then, build on recent findings
389 showing that rat and bat hippocampus contains cells whose firing rates encode the positions of
390 conspecifics in the environment. Specifically, we find that cells with similar functional properties
391 can be found in the human hippocampus, and moreover, that they can flexibly partition
392 information to achieve individuation.

393 We find evidence for two categories of cells, based on the shape of their tuning surface
394 for location (broad and narrow). The cells in the smaller cluster 2 have narrow highly localized
395 regions of strong activity, which give them a clear featural resemblance to place cells. However,
396 the cells in the larger cluster 1 have a distinct lack of localized tuning, but nonetheless still carry
397 information about spatial position. These cells have some resemblance to non-grid cells in the rat
398 entorhinal cortex, which were discovered using the same mapping algorithm we employ here
399 (Hardcastle et al., 2017 see also Diehl et al., 2017). Moreover, the category a cell falls in for self-
400 maps is generally the same category as it falls in for other maps, suggesting map shape may be
401 an intrinsic property of neurons, rather than an arbitrary feature. Surprisingly, the subspace semi-
402 orthogonalization appears mostly to be a property of the cluster 1 neurons, suggesting that an
403 overly strict focus on place-cells with focal tuning may result in ignoring important functional
404 features of hippocampal maps.

405 Our results show a modest but highly significant difference in the distribution of
406 functional cell types in the anterior (fewer cluster 2) and posterior (more cluster 2) hippocampus.
407 These results relate to ongoing discussions about the potential functional differences between
408 these regions (which are homologous to the rodent ventral and dorsal hippocampi, respectively,

409 Strange et al., 2014; To et al., 2024). The increased number of place-cell like coding in posterior
410 hippocampus, then, recapitulates known findings from rats (e.g., Jung et al., 1994; Kjelstrup et
411 al., 2018). Finally, the localization of partitioning to the more anterior cluster 1 neurons aligns
412 this part of the hippocampus with the kind of flexible adaptive cognition associated with
413 prefrontal cortex, with which anterior hippocampus has strong connections (Dalton et al., 2022).
414 Nonetheless, the differences we observe are modest, and, overall, our results endorse functional
415 continuity of the human hippocampus.

416 Our results relate to a previous series of three papers from our laboratory, in which
417 macaques performed a similar task (Yoo et al., 2020 and 2021B; Fine et al., 2024). In those
418 papers, we found that dorsal anterior cingulate cortex (dACC) actively predicts the future
419 position of pursued prey about 700 ms into the future (Yoo et al., 2020), also tracks a suite of
420 allocentric and egocentric variables related to the task (Yoo et al., 2021B), and corresponds with
421 inferred decision variables in the task (Fine et al., 2024). Relative to macaques, human behavior
422 is quite different - most critically, our macaque subjects needed at least three months to learn the
423 task, whereas humans need no training. Moreover, humans show evidence of highly efficient
424 behavioral strategies, such as cornering the prey, that macaques do not seem to learn, even with
425 months of training. In any case, our results here, focusing on the individuation problem, which
426 was not addressed in our earlier work, complement and extend our earlier findings.

427 We find it interesting that hippocampus actively tracks the position of the unpursued
428 prey. In our task, subjects typically select a single prey and pursue it for several seconds until
429 capture, leaving the other, unchosen one, ostensibly irrelevant. Nonetheless, from the perspective
430 of the hippocampus, this unselected prey shows only modest evidence of deprioritization.
431 (Namely, hippocampus still tracks the unpursued prey, although less robustly as it tracks the
432 pursued prey). The goal of the task is not, however, simply to track the preferred prey; instead
433 the player is allowed to switch to following the alternative (and sometimes does so, when, for
434 example, the unpursued prey comes nearby). Thus, from the perspective of choice, although not
435 behavior, monitoring the position of the unpursued prey is crucial: because switching is always a
436 possibility, continuing to focus on the pursued prey represents a decision to not switch. Our
437 results are reminiscent of theories in which the hippocampus maps potential alternatives to
438 current goals, rather than being limited to representing only the goals themselves.

439

REFERENCES

- 440
441 Barak, O., Rigotti, M., & Fusi, S. (2013). The sparseness of mixed selectivity neurons controls the
442 generalization–discrimination trade-off. *Journal of Neuroscience*, 33(9), 3844-3856.
443 Behrens, T. E., Muller, T. H., Whittington, J. C., Mark, S., Baram, A. B., Stachenfeld, K. L., & Kurth-
444 Nelson, Z. (2018). What is a cognitive map? Organizing knowledge for flexible behavior. *Neuron*,
445 100(2), 490-509.
446 Bernardi, S., Benna, M. K., Rigotti, M., Munuera, J., Fusi, S., & Salzman, C. D. (2020). The geometry of
447 abstraction in the hippocampus and prefrontal cortex. *Cell*, 183(4), 954-967.
448 Brown, T. I., Carr, V. A., LaRocque, K. F., Favila, S. E., Gordon, A. M., Bowles, B., ... & Wagner, A. D.
449 (2016). Prospective representation of navigational goals in the human hippocampus. *Science*,
450 352(6291), 1323-1326.
451 Burge, J., & Bonnen, K. (2025). Continuous psychophysics: past, present, future. *Trends in Cognitive
452 Sciences*.
453 Cervera, R. L., Wang, M. Z., & Hayden, B. Y. (2020). Systems neuroscience of curiosity. *Current Opinion
454 in Behavioral Sciences*, 35, 48-55.
455 Chaure, F. J., Rey, H. G. & Quian Quiroga, R. A novel and fully automatic spike-sorting implementation
456 with variable number of features. *J Neurophysiol* 120, 1859–1871 (2018).
457 Chersi, F., & Burgess, N. (2015). The cognitive architecture of spatial navigation: hippocampal and
458 striatal contributions. *Neuron*, 88(1), 64-77.
459 Cisek, P., & Kalaska, J. F. (2010). Neural mechanisms for interacting with a world full of action choices.
460 Annual review of neuroscience, 33(1), 269-298.
461 Dale, A.M., Fischl, B., Sereno, M.I., 1999. Cortical surface-based analysis. I. Segmentation and surface
462 reconstruction. *Neuroimage* 9, 179-194.
463 Dalton, M. A., D'Souza, A., Lv, J., & Calamante, F. (2022). New insights into anatomical connectivity
464 along the anterior–posterior axis of the human hippocampus using *in vivo* quantitative fibre
465 tracking. *elife*, 11, e76143.
466 Danjo, T., Toyoizumi, T., & Fujisawa, S. (2018). Spatial representations of self and other in the
467 hippocampus. *Science*, 359(6372), 213-218.
468 Diehl, G. W., Hon, O. J., Leutgeb, S., & Leutgeb, J. K. (2017). Grid and nongrid cells in medial entorhinal
469 cortex represent spatial location and environmental features with complementary coding
470 schemes. *Neuron*, 94(1), 83-92.
471 Ebitz, R. B., & Hayden, B. Y. (2021). The population doctrine in cognitive neuroscience. *Neuron*, 109(19),
472 3055-3068.
473 Ebitz, R. B., Sleezer, B. J., Jedema, H. P., Bradberry, C. W., & Hayden, B. Y. (2019). Tonic exploration
474 governs both flexibility and lapses. *PLoS computational biology*, 15(11), e1007475.
475 Eisenreich, B. R., Hayden, B. Y., & Zimmermann, J. (2019). Macaques are risk-averse in a freely moving
476 foraging task. *Scientific reports*, 9(1), 15091.
477 Ekstrom, A. D., Kahana, M. J., Caplan, J. B., Fields, T. A., Isham, E. A., Newman, E. L., & Fried, I.
478 (2003). Cellular networks underlying human spatial navigation. *Nature*, 425(6954), 184-188.
479 Elsayed, G. F., Lara, A. H., Kaufman, M. T., Churchland, M. M., & Cunningham, J. P. (2016).
480 Reorganization between preparatory and movement population responses in motor cortex.
481 *Nature communications*, 7(1), 13239.
482 Epstein, R. A., Patai, E. Z., Julian, J. B., & Spiers, H. J. (2017). The cognitive map in humans: spatial
483 navigation and beyond. *Nature neuroscience*, 20(11), 1504-1513.
484 Fabian, S. T., Sumner, M. E., Wardill, T. J., Rossoni, S., & Gonzalez-Bellido, P. T. (2018). Interception by
485 two predatory fly species is explained by a proportional navigation feedback controller. *Journal of
486 The Royal Society Interface*, 15(147), 20180466.

- 487 Fenton, A. A., & Muller, R. U. (1998). Place cell discharge is extremely variable during individual passes
488 of the rat through the firing field. *Proceedings of the National Academy of Sciences*, 95(6), 3182-
489 3187.
- 490 Fine, J. M., Maisson, D. J. N., Yoo, S. B. M., Cash-Padgett, T. V., Wang, M. Z., Zimmermann, J., &
491 Hayden, B. Y. (2023). Abstract value encoding in neural populations but not single neurons.
492 *Journal of Neuroscience*, 43(25), 4650-4663.
- 493 Fine, J. M., Yoo, S. B. M., & Hayden, B. Y. (2024). Control over a mixture of policies determines change
494 of mind topology during continuous choice. *bioRxiv*, 2024-04.
- 495 Forli, A., & Yartsev, M. M. (2023). Hippocampal representation during collective spatial behaviour in bats.
496 *Nature*, 621(7980), 796-803.
- 497 Freesurfer: <https://freesurfer.net/fswiki/FreeSurferMethodsCitation>
- 498 Fusi, S., Miller, E. K., & Rigotti, M. (2016). Why neurons mix: high dimensionality for higher cognition.
499 *Current opinion in neurobiology*, 37, 66-74.
- 500 Gauthier, J. L., & Tank, D. W. (2018). A dedicated population for reward coding in the hippocampus.
501 *Neuron*, 99(1), 179-193.
- 502 Gordon, J., Maselli, A., Lancia, G. L., Thiery, T., Cisek, P., & Pezzulo, G. (2021). The road towards
503 understanding embodied decisions. *Neuroscience & Biobehavioral Reviews*, 131, 722-736.
- 504 Groppe DM, Bickel S, Dykstra AR, et al. iELVis: An open source MATLAB toolbox for localizing and
505 visualizing human intracranial electrode data. *J Neurosci Methods*. 2017;281:40-48.
- 506 Hardcastle, K., Maheswaranathan, N., Ganguli, S., & Giocomo, L. M. (2017). A multiplexed,
507 heterogeneous, and adaptive code for navigation in medial entorhinal cortex. *Neuron*, 94(2), 375-
508 387.
- 509 Hart, P. E. & Nils, J. Formal basis for the heuristic determination of minumum cost path. *IEEE Trans.*
510 *Syst. Sci. Cyber.* 4, 100–107 (1968).
- 511 Harvey, C. D., Collman, F., Dombeck, D. A., & Tank, D. W. (2009). Intracellular dynamics of hippocampal
512 place cells during virtual navigation. *Nature*, 461(7266), 941-946.
- 513 Hayden, B. Y. (2019). Why has evolution not selected for perfect self-control?. *Philosophical Transactions*
514 *of the Royal Society B*, 374(1766), 20180139.
- 515 Jacobs, Joshua, Michael J. Kahana, Arne D. Ekstrom, Matthew V. Mollison, and Itzhak Fried. "A sense of
516 direction in human entorhinal cortex." *Proceedings of the National Academy of Sciences* 107, no.
517 14 (2010): 6487-6492.
- 518 Jenkinson, M., Bannister, P., Brady, J. M. and Smith, S. M. 2002. Improved Optimisation for the Robust
519 and Accurate Linear Registration and Motion Correction of Brain Images. *NeuroImage*, 17(2),
520 825-841.
- 521 Jenkinson, M., & Smith, S. (2001). A global optimisation method for robust affine registration of brain
522 images. *Medical image analysis*, 5(2), 143-156.
- 523 Johnston, W. J., Fine, J. M., Yoo, S. B. M., Ebitz, R. B., & Hayden, B. Y. (2024). Semi-orthogonal
524 subspaces for value mediate a binding and generalization trade-off. *Nature Neuroscience*, 27(11),
525 2218-2230.
- 526 Joshi, A., Scheinost, D., Okuda, H., Belhachemi, D., Murphy, I., Staib, L. H., & Papademetris, X. (2011).
527 Unified framework for development, deployment and robust testing of neuroimaging algorithms.
528 *Neuroinformatics*, 9(1), 69-84.
- 529 Jung, M. W., Wiener, S. I., & McNaughton, B. L. (1994). Comparison of spatial firing characteristics of
530 units in dorsal and ventral hippocampus of the rat. *Journal of Neuroscience*, 14(12), 7347-7356.
- 531 Kaufman, M. T., Benna, M. K., Rigotti, M., Stefanini, F., Fusi, S., & Churchland, A. K. (2022). The
532 implications of categorical and category-free mixed selectivity on representational geometries.
533 *Current opinion in neurobiology*, 77, 102644.
- 534 Kjelstrup, K. B., Solstad, T., Brun, V. H., Hafting, T., Leutgeb, S., Witter, M. P., ... & Moser, M. B. (2008).
535 Finite scale of spatial representation in the hippocampus. *Science*, 321(5885), 140-143.

- 536 Koch, J., Demirel, M. C., & Stisen, S. (2018). The SPAatial EFficiency metric (SPAEF): Multiple-
537 component evaluation of spatial patterns for optimization of hydrological models. *Geoscientific
538 Model Development*, 11(5), 1873-1886.
- 539 Kunz, L., Brandt, A., Reinacher, P. C., Staresina, B. P., Reifenstein, E. T., Weidemann, C. T., ... &
540 Jacobs, J. (2021). A neural code for egocentric spatial maps in the human medial temporal lobe.
541 *Neuron*, 109(17), 2781-2796.
- 542 Li X, Morgan PS, Ashburner J, Smith J, Rorden C (2016) The first step for neuroimaging data analysis:
543 DICOM to NIfTI conversion. *J Neurosci Methods*. 264:47-56. doi:
544 10.1016/j.jneumeth.2016.03.001. PMID: 26945974
- 545 Mackay, S., Reber, T. P., Bausch, M., Boström, J., Elger, C. E., & Mormann, F. (2024). Concept and
546 location neurons in the human brain provide the 'what' and 'where' in memory formation. *Nature
547 Communications*, 15(1), 7926.
- 548 Magnotti JF, Wang Z, Beauchamp MS. RAVE: comprehensive open-source software for reproducible
549 analysis and visualization of intracranial EEG data. *NeuroImage* (2020) 223:117341.
- 550 Maguire, E. A., Woollett, K., & Spiers, H. J. (2006). London taxi drivers and bus drivers: a structural MRI
551 and neuropsychological analysis. *Hippocampus*, 16(12), 1091-1101.
- 552 Martinez-Trujillo, J. (2025). Why do primates have view cells instead of place cells?. *Trends in Cognitive
553 Sciences*.
- 554 Merel, J., Botvinick, M., & Wayne, G. (2019). Hierarchical motor control in mammals and machines.
555 *Nature communications*, 10(1), 5489.
- 556 Miller, J. F., Neufang, M., Solway, A., Brandt, A., Trippel, M., Mader, I., ... & Schulze-Bonhage, A. (2013).
557 Neural activity in human hippocampal formation reveals the spatial context of retrieved memories.
558 *Science*, 342(6162), 1111-1114.
- 559 Nyberg, N., Duvelle, É., Barry, C., & Spiers, H. J. (2022). Spatial goal coding in the hippocampal
560 formation. *Neuron*, 110(3), 394-422.
- 561 O'Keefe, J., Burgess, N., Donnett, J. G., Jeffery, K. J., & Maguire, E. A. (1998). Place cells, navigational
562 accuracy, and the human hippocampus. *Philosophical Transactions of the Royal Society of
563 London*.
- 564 O'Keefe, J., & Dostrovsky, J. (1971). The hippocampus as a spatial map: preliminary evidence from unit
565 activity in the freely-moving rat. *Brain research*.
- 566 Olberg, R. M., Worthington, A. H., & Venator, K. R. (2000). Prey pursuit and interception in dragonflies.
567 *Journal of Comparative Physiology A*, 186, 155-162.
- 568 Omer, D. B., Maimon, S. R., Las, L., & Ulanovsky, N. (2018). Social place-cells in the bat hippocampus.
569 *Science*, 359(6372), 218-224.
- 570 Panichello, M. F., & Buschman, T. J. (2021). Shared mechanisms underlie the control of working memory
571 and attention. *Nature*, 592(7855), 601-605.
- 572 Parthasarathy, A., Herikstad, R., Bong, J. H., Medina, F. S., Libedinsky, C., & Yen, S. C. (2017). Mixed
573 selectivity morphs population codes in prefrontal cortex. *Nature neuroscience*, 20(12), 1770-1779.
- 574 Pillow, J. W. et al. Spatio-temporal correlations and visual signalling in a complete neuronal population.
575 *Nature* 454, 995–999 (2008).
- 576 Poppenk, J., Evensmoen, H. R., Moscovitch, M., & Nadel, L. (2013). Long-axis specialization of the
577 human hippocampus. *Trends in cognitive sciences*, 17(5), 230-240.
- 578 Poucet, B., & Hok, V. (2017). Remembering goal locations. *Current opinion in behavioral sciences*, 17,
579 51-56.
- 580 Rao, R. P., von Heimendahl, M., Bahr, V., & Brecht, M. (2019). Neuronal responses to conspecifics in the
581 ventral CA1. *Cell reports*, 27(12), 3460-3472. Forli, A., & Yartsev, M. M. (2023). Hippocampal
582 representation during collective spatial behaviour in bats. *Nature*, 621(7980), 796-803.
- 583 Rigotti, M., Barak, O., Warden, M. R., Wang, X. J., Daw, N. D., Miller, E. K., & Fusi, S. (2013). The
584 importance of mixed selectivity in complex cognitive tasks. *Nature*, 497(7451), 585-590.

- 585 Rousseeuw, P. J. (1987). Silhouettes: a graphical aid to the interpretation and validation of cluster
586 analysis. *Journal of computational and applied mathematics*, 20, 53-65.
- 587 Skaggs, W., Mcnaughton, B., & Gothard, K. (1992). An information-theoretic approach to deciphering the
588 hippocampal code. *Advances in neural information processing systems*, 5.
- 589 Stangl, M., Topalovic, U., Inman, C. S., Hiller, S., Villaroman, D., Aghajan, Z. M., ... & Suthana, N. (2021).
590 Boundary-anchored neural mechanisms of location-encoding for self and others. *Nature*,
591 589(7842), 420-425.
- 592 Stephens, D. W., & Krebs, J. R. (1986). *Foraging theory* (Vol. 6). Princeton university press.
- 593 Strange, B. A., Witter, M. P., Lein, E. S., & Moser, E. I. (2014). Functional organization of the
594 hippocampal longitudinal axis. *Nature reviews neuroscience*, 15(10), 655-669.
- 595 Suthana, N. A., Ekstrom, A. D., Moshirvaziri, S., Knowlton, B., & Bookheimer, S. Y. (2009). Human
596 hippocampal CA1 involvement during allocentric encoding of spatial information. *Journal of
597 Neuroscience*, 29(34), 10512-10519.
- 598 Tang, C., Herikstad, R., Parthasarathy, A., Libedinsky, C., & Yen, S. C. (2020). Minimally dependent
599 activity subspaces for working memory and motor preparation in the lateral prefrontal cortex.
600 *Elife*, 9, e58154.
- 601 To, T. V., Wang, D. X., Wolfe, C. B., & Lega, B. C. (2024). Neurophysiological Evidence of Human
602 Hippocampal Longitudinal Differentiation in Associative Memory.
- 603 Tye, K. M., Miller, E. K., Taschbach, F. H., Benna, M. K., Rigotti, M., & Fusi, S. (2024). Mixed selectivity:
604 Cellular computations for complexity. *Neuron*, 112(14), 2289-2303.
- 605 Wang, M. Z., & Hayden, B. Y. (2021). Latent learning, cognitive maps, and curiosity. *Current Opinion in
606 Behavioral Sciences*, 38, 1-7.
- 607 Watrous, A. J., Miller, J., Qasim, S. E., Fried, I., & Jacobs, J. (2018). Phase-tuned neuronal firing
608 encodes human contextual representations for navigational goals. *Elife*, 7, e32554.
- 609 Wilson, M. A., & McNaughton, B. L. (1993). Dynamics of the hippocampal ensemble code for space.
610 *Science*, 261(5124), 1055-1058.
- 611 Xie, Y., Hu, P., Li, J., Chen, J., Song, W., Wang, X. J., ... & Wang, L. (2022). Geometry of sequence
612 working memory in macaque prefrontal cortex. *Science*, 375(6581), 632-639.
- 613 Yacoub, E., Grier, M. D., Auerbach, E. J., Lagore, R. L., Harel, N., Adriany, G., ... & Zimmermann, J.
614 (2020). Ultra-high field (10.5 T) resting state fMRI in the macaque. *Neuroimage*, 223, 117349.
- 615 Yang, A. I., Wang, X., Doyle, W. K., Halgren, E., Carlson, C., Belcher, T. L., et al. (2012). Localization of
616 dense intracranial electrode arrays using magnetic resonance imaging. *NeuroImage* 63(1), 157–
617 165. doi:10.1016/j.neuroimage.2012.06.039
- 618 Ydenberg, R. C., & Dill, L. M. (1986). The economics of fleeing from predators. In *Advances in the Study
619 of Behavior* (Vol. 16, pp. 229-249). Academic Press.
- 620 Yoo, S. B. M., Tu, J. C., Piantadosi, S. T., & Hayden, B. Y. (2020). The neural basis of predictive pursuit.
621 *Nature neuroscience*, 23(2), 252-259.
- 622 Yoo, S. B. M., Hayden, B. Y., & Pearson, J. M. (2021A). Continuous decisions. *Philosophical
623 Transactions of the Royal Society B*, 376(1819), 20190664.
- 624 Yoo, S. B. M., Tu, J. C., & Hayden, B. Y. (2021B). Multicentric tracking of multiple agents by anterior
625 cingulate cortex during pursuit and evasion. *Nature communications*, 12(1), 1985.
- 626 Yoo, S. B. M., & Hayden, B. Y. (2020). The transition from evaluation to selection involves neural
627 subspace reorganization in core reward regions. *Neuron*, 105(4), 712-724.
- 628 Zhang, X., Cao, Q., Gao, K., Chen, C., Cheng, S., Li, A., ... & Miao, C. (2024). Multiplexed representation
629 of others in the hippocampal CA1 subfield of female mice. *Nature Communications*, 15(1), 3702.
- 630
- 631 URL for Supplementary Video: https://www.youtube.com/watch?v=qR_54WB9Xpl

632

633

634 *Human intracranial neurophysiology*

635 Experimental data were recorded from 13 adult patients (6 males and 7 females)
636 undergoing intracranial monitoring for epilepsy. The hippocampus was not a seizure
637 focus area of any patients included in the study. Single neuron data were recorded from
638 stereotactic (sEEG) probes, specifically AdTech Medical probes in a Behnke-Fried
639 configuration. Each patient had an average of 3 probes terminating in left and right
640 hippocampus. Electrode locations are verified by co-registered pre-operative MRI and
641 post-operative CT scans. Each probe includes 8 microwires, each with 8 contacts,
642 specifically designed for recording single-neuron activity. Single neuron data were
643 recorded using a 512-channel Blackrock Microsystems Neuroport system sampled at 30
644 kHz. To identify single neuron action potentials, the raw traces were spike-sorted using
645 the WaveClus sorting algorithm (Choure et al., 2018) and then manually evaluated. Noise
646 was removed and each signal was classified as multi or single unit using several
647 criteria: consistent spike waveforms, waveform shape (slope, amplitude, trough-to-
648 peak), and exponentially decaying ISI histogram with no ISI shorter than the refractory
649 period (1 ms). The analyses here used only single unit activity.

650

651 *Electrode visualization*

652 Electrodes were localized using the software pipeline intracranial Electrode
653 Visualization (iELVis, Groppe et al., 2017) and plotted across patients on an average
654 brain using Reproducible Analysis & Visualization of iEEG (RAVE, Magnotti et al.,
655 2020). For each patient, DICOM images of the preoperative T1 anatomical MRI and the
656 postoperative Stealth CT scans were acquired and converted to NIfTI format (Li et al.,
657 2016). The CT was aligned to MRI space using FSL (Jenkinson and Smith, 2001;
658 Jenkinson et al, 2002). The resulting coregistered CT was loaded into BioImage Suite
659 (version 3.5β1) (Joshi et al., 2001) and the electrode contacts were manually localized.
660 Electrodes coordinates were converted to patient native space using iELVis MATLAB
661 functions (Joshi et al., 2011; Yang et al., 2012) and plotted on the Freesurfer (version
662 7.4.1, Dale et al., 1999) reconstructed brain surface. Microelectrode coordinates are
663 taken from the first (deepest) macro contact on the Ad-Tech Behnke Fried depth
664 electrodes. RAVE was used to transform each patient's brain and electrode coordinates
665 into MNI152 average space (Magnotti et al., 2020). The average coordinates were
666 plotted together on a glass brain with the hippocampus segmentation and colored by
667 location within the hippocampus.

668

669 *The prey-pursuit task*

670 The task used here is similar but not identical to one we have previously used in
671 macaques (Yoo et al., 2020A and 2021; Fine et al., 2024; **Supplementary Video**). At
672 the beginning of each trial, two shapes appeared on a gray background (RGB:
673 128/128/128) on a standard computer monitor placed in front of the subject. A yellow
674 circle (15-pixels in diameter) was an avatar for the research participant. Its position was
675 determined by the joystick and was limited by the screen boundaries. A square shape
676 (30 pixels in length) represented the prey. The movement of the prey was determined
677 by a simple artificial intelligence algorithm (see below). Each trial ended with either the
678 successful capture of the prey or after 20 sec, whichever came first. Successful capture

679 was defined as any spatial overlap between the avatar circle and the prey square.
680 Capture resulted in scored points; the number of points corresponded to prey color as
681 follows: 1 point for orange; 3 points for green; 5 points for cyan.

682 The path of the prey was generated interactively using A-star pathfinding
683 methods, which are commonly used in video gaming (Hart & Nils, 1968). For every
684 frame (16.67 ms), we computed the cost of 15 possible future positions the prey could
685 move to in the next time-step. These 15 positions were equally spaced on the
686 circumference of a circle centered on the current position of the prey, with a radius
687 equal to the maximum distance the prey could travel within one time-step. The cost in
688 turn was based on the following two factors: the position in the field and the position of
689 the avatar of the subject. The field that the prey moved in had a built-in bias for cost,
690 which made the prey more likely to move toward the center. The cost due to distance
691 from the avatar of the subject was transformed using a sigmoidal function: the cost
692 became zero beyond a certain distance so that the prey did not move, and it became
693 greater as distance from the avatar of the subject decreased. Eventually, the costs from
694 these 15 positions were calculated and the position with the lowest cost was selected
695 for the next movement. If the next movement was beyond the screen range (1,800 ×
696 1,000 resolution), then the position with the second lowest cost was selected, and so
697 on.

698 The maximum speed of the participant was 23 pixels per frame (and each frame
699 was 16.67 ms). The maximum and minimum speeds of the prey remained the same
700 across subjects. In trials with predators, a predator (triangle shape) appeared on 50% of
701 trials. Capture by the predator led to points loss. Predators came in five different types
702 (indicated by color) indicating different levels of points loss, ranging from 1 to 5 points.
703 The algorithm of the predator is to minimize the distance between itself and player.
704 Unlike the prey, the predator algorithm is governed by this single rule. The design of the
705 task reflects primarily the desire to have a rich and variegated virtual world with
706 opportunities for choices at multiple levels that is neither trivially simple nor overly
707 complex.

708

709 *Task presentation*

710 Patients played at least 100 trials (average 119 trials) of the prey-pursuit task
711 using a joystick (**Figure 1A, B**). The joystick was a commercially available joystick with
712 a built-in potentiometer (Logitech Extreme Pro 3D). The joystick position was read out
713 by a custom-coded program in Matlab running on the stimulus-control computer. The
714 joystick was controlled by an algorithm that detected the positional change of the
715 joystick and limited the maximum pixel movement to within 23 pixels in 16.67 ms. Task
716 events were synchronized to the neural recording system via comments, sent through
717 analog port, from the computer playing the task to the Neural Signal Processor (NSP) at
718 30 kHz.

719

720 *Linear–nonlinear model (LN-GLM)*.

721 To test the selectivity of neurons for various experimental variables, we
722 constructed GLMs with navigational variables (Hardcastle et al., 2017; Pillow et al.,
723 2008). The GLMs estimated the spike rate of one neuron during time bin t as an
724 exponential function of the weighted sum of the relevant value of each variable at time t ,

725 for which the weights are determined by a set of coefficients (w_i). The estimated firing
726 rates from the GLMs can be expressed as follows:
727

728
$$r = \exp(\sum X_i^T w_i)/dt$$

729

730 Where r denotes a vector of firing rates for one neuron over T time points across the
731 session, and i indexes the variables of interest, for example, the position of the avatar
732 on the screen. The vector of firing rates over T time points provide the benefit for
733 modeling the neural activity without the need of specifically timelocking to a behavioral
734 event. X_i is a matrix in which each column represents a set of ‘state variables’ of the
735 subject obtained from binning the continuous variable so that all the columns for a
736 particular row are 0, except for one column. In this case, state variables were obtained
737 binning the position of self and prey over a 6x6 grid (36 bins). As a result, each neuron
738 was assigned a design matrix with rows corresponding to the number of samples and
739 columns corresponding to the number of bins.

740 Unlike conventional tuning curve analysis, GLM analysis does not assume the
741 parametric shape of the tuning curve a priori. Instead, the weights, which define the
742 shape of tuning for each neuron, were optimized by maximizing the Poisson log-
743 likelihood of the observed spike train given the model-expected spike number, with
744 additional regularization for the smoothness of parameters in a continuous variable, and
745 a lasso regularization for parameters in a discrete variable. Position parameters were
746 separately smoothed across rows and columns. The regularization hyperparameter was
747 chosen by maximizing the cross-validation log-likelihood based on several randomly
748 selected neurons. The unconstrained optimization with gradient and Hessian was
749 performed (Matlab fminunc function). The model performance of each neuron was
750 quantified by the log-likelihood of held out data under the model (**Figure 2C**). This
751 cross-validation procedure was repeated ten times (tenfold cross-validation), and
752 overfitting was penalized. Through multiple levels of penalties, we compared the
753 performance of models with varying complexity.
754
755
756

757 *Forward model selection*

758 Model selection was based on the cross-validated log-likelihood value for each
759 model. We first fit n models with a single variable, where n is the total number of
760 variables. The best single model was determined by the largest increase in spike-
761 normalized log-likelihood from the null model (that is, the model with a single parameter
762 representing the mean firing rate). Then, additional variables ($n - 1$ in total) were added
763 to the best single variable model. The best two variable model was preferred over the
764 single variable model only if it significantly improved the cross-validation log-likelihood
765 value (Wilcoxon signed-rank test, $\alpha = 0.05$). Likewise, the procedure was continued for
766 the three-variable model and beyond if adding more variables significantly improved the
767 model performance, and the best, simplest model was selected. The cell was
768 categorized as not tuned to any of the variables considered if the log-likelihood increase
769 was not significantly higher than baseline, which was the mean firing rate of fitted
770 neurons across the session.

771

772 *Spatial similarity index (SPAEC)*

773 To compare the similarity between two spatial representations, we used the
774 spatial efficiency measure (SPAEC) that prior literature suggests to be more robust than
775 the 2D spatial correlation (Koch et al, 2018). It quantifies the similarity between two
776 maps as follows:

777

778
$$\text{SPAEC} = 1 - \sqrt{(A - 1)^2 + (B - 1)^2 + (C - 1)^2}$$

779

780 where A is the Pearson correlation between two maps, B is the ratio between the
781 coefficients of variation for each map and C is the activity similarity measured by
782 histogram profiles. Values near -1 indicate anticorrelated maps (one tends to be high
783 when the other is low), 0 indicates uncorrelated maps and 1 indicates perfect matching
784 between the two. By definition, SPAEC is not strictly constrained between -1 and 1.
785 However, values outside this range tend to be rare, and in any case, in our data, values
786 outside this interval never occurred.

787 To determine if the SPAEC values were significantly different from zero, we built
788 a shuffled distribution over 1000 permutations. We then used a two-sided test to extract
789 p-values, considering significance at $p < 0.05$. To determine the noise ceiling, we
790 performed 1000 within-agent half-splits. That is, for each iteration and each neuron, we
791 randomly split the trials for each agent into two independent halves, computed the
792 spatial tuning maps separately for each half, and then measured the spatial similarity
793 between the two resulting maps. This process estimates the upper bound of explainable
794 variance by accounting for the inherent noise in the data, providing a reference against
795 which observed spatial similarities can be compared.

796

797 *K-means clustering and Principal Component Analysis*

798 For this analysis, we included the entire neuronal population (390 neurons). We
799 computed spatial tuning curves for each neuron based on the positions of the self and
800 chosen prey. The task space (computer monitor) was divided into a 6×6 grid, resulting
801 in a 36-bin tuning curve for each neuron per agent. Each tuning curve was then
802 normalized between 0 and 1 on a per-neuron basis, by dividing by the maximum value
803 of the respective neuron's tuning curve. This ensured that differences in firing rates did
804 not bias our subsequent analyses. We then applied the k-means clustering algorithm to
805 the normalized tuning curves. Clustering was performed separately for self-position
806 tuning curves and chosen prey-position tuning curves. To determine the optimal number
807 of clusters we used silhouette values, which assess clustering quality by measuring how
808 well each data point fits within its assigned cluster relative to other clusters. A silhouette
809 score closer to -1 indicates potential misclassification, while a score closer to +1
810 suggests strong cluster cohesion and clear separation from other clusters (Rousseeuw,
811 1986). We selected the number of clusters that maximized the silhouette value, which
812 turned out to be two for both self and chosen prey position tuning curves. Thus we could
813 classify each neuron as belonging to cluster 1 or cluster 2.

814

815 We then performed principal component analysis (PCA) to visualize how the
816 structure of the spatial tuning curves varies across neurons. That is, identifying the main
patterns of variability in neurons' responses to different positions. PCA was applied to

817 the same normalized tuning curves (*neurons × bins* matrix) used for k-means clustering,
818 where each row represented a neuron and each column corresponded to a spatial bin in
819 its tuning curve. The resulting principal components (PCs) captured different aspects of
820 tuning variability across the population.

821 To visualize this structure, we plotted neurons in the PCA space using their PC1
822 and PC2 scores and colored them according to their k-means cluster assignment. This
823 allowed us to assess whether neurons with similar tuning properties grouped together in
824 the PCA-defined space.

825 Specifically, we applied PCA separately to the self-position tuning maps and the
826 chosen prey tuning maps, coloring neurons according to their respective k-means
827 clustering results (**Figure 3C, D**). Lastly, we re-applied PCA to the chosen prey tuning
828 maps and colored neurons by cross-referencing their cluster identities from both self
829 and chosen prey tuning maps (**Figure 3E**). This final analysis highlighted differences in
830 cluster membership between self and chosen prey tuning representations.
831

832 *Information per spike and SNR*

833 This analysis was conducted on the raw (non-normalized) self-position spatial
834 tuning curves (again 36 bins were used). Each neuron was assigned a cluster identity
835 based on the results of k-means clustering applied to the self-position tuning curves. We
836 calculated the spatial information per spike as the mutual information between the
837 spatial location and the spike train, computed as:
838

$$839 I = \sum p_i \left(\frac{r_i}{r} \right) \log_2 \left(\frac{r_i}{r} \right)$$

840 Where r_i is the firing rate of each spatial bin (36 bins total) for neuron n , r is the average
841 firing rate across all bins, and p_i is the probability of occupying each spatial bin (Skaggs
842 et al., 1992). In our case, since participants were able to sample the whole task space
843 (**Figure 1B, C** and **Figure 3A**), we assumed uniform occupancy.
844

845 To assess the stability of cells firing, we calculate the signal-to-noise ratio (SNR),
846 defined as the variance in the mean firing rate across bins divided by the mean rate
847 itself. This metric provides a measure of the consistency of spatial encoding (Fenton
848 and Muller, 1998).

849

$$850 \text{SNR} = \frac{\text{variance of mean tuning curve}}{\text{mean firing rate}}$$

851 Higher SNR signifies consistency in firing across spatial locations, while lower
852 SNR indicates less spatially structured responses. Significance of differences between
853 groups was assessed using a non-parametric Wilcoxon rank-sum test.
854

855 *Spatial similarity matrix*

856 To represent the correlation structure of self and prey representations, we
857 constructed an $N \times N$ matrix for each agent, with N number of neurons. Each matrix entry
858 represents the spatial similarity between the spatial maps of neuron pairs. Spatial maps
859 were normalized between 0 and 1. The spatial similarity matrix is symmetric and
860 contains values between -1 and +1.
861

862 For visualization purposes only, we applied hierarchical clustering to the self
863 spatial similarity matrix. Specifically, we defined the dissimilarity self matrix as *1-spatial*
864 *similarity matrix* and then applied the clustering algorithm using average linkage
865 method. The extracted indices were then used to sort the matrices for the remaining
866 agents (chosen and unchosen prey).

867

868 *Pairwise correlations*

869 To compute the pairwise correlations between spatial similarity matrices, we
870 used Pearson's correlation coefficient. We assessed significance constructing a null
871 distribution over 500 permutations. We then used a two-sided test to extract p-values,
872 with significance considered at $p < 0.05$

873

874 *Neural subspaces analysis*

875 We performed PCA on the spatial similarity matrix by treating the self spatial
876 similarity matrix as a covariance-like matrix and applying eigendecomposition. However,
877 this matrix was not positive semi-definite (PSD). To approximate it to its nearest PSD
878 form, we performed eigendecomposition and set negative eigenvalues to zero. We then
879 identified the principal components (PCs) through a second eigendecomposition. Each
880 identified self-PC represents an orthogonal direction in the N-dimensional neural space.

881 We then projected the prey spatial similarity matrices onto the self-PCs and
882 quantified the percent of variance explained relative to the total variance of the self
883 spatial similarity matrix (**Figure 4I, J**; green and grey bars). This procedure reveals the
884 amount of self and prey variance shared in the self-PCs. Thus, if self and prey maps
885 occupied semi-orthogonal subspaces, self-PCs would capture little variance from prey
886 maps. Conversely, if the maps shared collinear subspaces, self-PCs would generalize
887 across agents, explaining significant variance from prey representations.

888 To assess significance, we divided the neural data for each neuron into two
889 halves (500 splits). For each split, spatial tuning curves were computed separately for
890 each agent using one half of the data. We constructed the spatial similarity matrix, and
891 identified the top self-PCs for the self training set (half 1). We then projected the self
892 and prey maps onto the self PCs (halves 2 projected onto self half 1). The distribution of
893 variance explained from within-self projections served as an estimate of noise ceiling.
894 The variability of variance explained in within- and cross-condition projections (chosen
895 prey and unchosen prey onto self-PCs) provides confidence intervals estimates.
896 Variance explained in cross-condition projections was statistically compared to noise
897 ceiling (assessed from the within-self variance distribution) using paired tests with
898 Bonferroni correction.

899 Last, to quantify the degree of subspace orthogonality, we performed
900 eigendecomposition on both the self and prey similarity matrices to identify the top self-
901 and prey- PCs. We computed the angle between corresponding PCs using cosine
902 similarity. Cosine similarity measures the cosine of the angle between two vectors,
903 capturing their directional alignment in high-dimensional space. To determine statistical
904 significance, we generated a null distribution via 500 permutations and computed
905 permutation-based p-values using a two-tailed test, considering $p < 0.05$ as significant.